Non-micelle-like Amyloid Aggregate Stabilizes Amyloid β (1-42) Growth Nuclei Formation

Running Title: Roles of aggregate milieu for the fibril formation

Ikuo Kurisaki[*1], Shigenori Tanaka[*2]

[1]Waseda Research Institute for Science and Engineering, Waseda University, Research Innovation Center, 513 Tsurumaki-cho, Waseda, Shinjuku-ku, Tokyo 169-8555, Japan

[2]Department of Computational Science, Graduate School of System Informatics, Kobe University, 1-1 Rokkodai-cho, Nada-ku, Kobe, Hyogo 657-8501, Japan

[*]Ikuo Kurisaki

E-mail: ikuo.kurisaki@aoni.waseda.jp, Tel: +81-3-6380-2472

[*]Shigenori Tanaka

E-mail: tanaka2@kobe-u.ac.jp, Tel: +81-78-803-6620

Data availability statement

The data that support the findings of this study are available from the corresponding authors upon reasonable request.

Funding statement

This work was supported by a Grant-Aid for Scientific Research on Innovative Areas "Chemistry for Multimolecular Crowding Biosystems" (JSPS KAKENHI Grant No. JP17H06353) and by MEXT Quantum Leap Flagship Program (Grant No. JPMXS0120330644)

Ethics approval statement

None.

Patient consent statement

None.

Permission to reproduce material from other sources

There are no reproduced materials from other sources. All of the materials were newly

created for this manuscript.

Clinical trial registration

None.

Conflicts of interest disclosure

The authors declare no competing financial interest.

Abstract

Protein aggregate formations are essential processes to regulate biochemical networks in the cell, while anomalously formed aggregates such as amyloid fibrils cause serious neuronal diseases. It has been discussed for a quarter century that protein crowding milieus, such as micelle-like aggregates, promote the formation of growth nuclei, fibril-growth competent aggregates which trigger rapid growth of pathogenic amyloid fibrils, but the mechanisms are still elusive, in particular at microscopic level. In this study, we examined the long-standing problem by employing atomistic molecular dynamics simulations for amyloid β(1-42) ($A\beta_{42}$), the paradigmatic amyloid-forming peptide. First, we constructed an atomistic model of $A\beta_{42}$ growth nuclei in $A\beta_{42}$ aggregate milieu, the pentameric $A\beta_{42}$ protomer dimer surrounded by 40 $A\beta_{42}$ monomers. Next, we simulated $A\beta_{42}$ monomer dissociation from the $A\beta_{42}$ growth nuclei and examined the effect of $A\beta_{42}$ aggregate milieu on the process. $A\beta_{42}$ aggregates spatially restrict $A\beta_{42}$ monomer dissociation pathways, while such spatial restriction itself does not significantly suppress $A\beta_{42}$ monomer dissociation from the growth nuclei. Rather, $A\beta_{42}$ aggregate milieus thermodynamically stabilize an $A\beta_{42}$ monomer binding to the growth edge by making atomic contacts with the monomer and contributes to stable formation of growth nuclei. A part of the aggregate milieu anchors dissociating monomer to the remaining part of

growth nuclei, suggesting cooperative suppression of $A\beta_{42}$ monomer dissociation from $A\beta_{42}$ growth nuclei. Since the $A\beta_{42}$ aggregate milieu does not take a micelle-like configuration, we here discuss a new mechanism for stable formation of $A\beta_{42}$ growth nuclei in the presence of aggregate milieu.

Keywords: amyloid-β (1–42), amyloid fibril formation, protein aggregate, molecular dynamics simulations, thermodynamic stability, growth nuclei

Abbreviations: amyloid protein, amyloid-β (1-42) ($A\beta_{42}$); cryogenic electron microscopy (cryo-EM); molecular mechanics (MM); molecular dynamics (MD); steered molecular dynamics (SMD); umbrella sampling molecular dynamics (USMD); potential of mean force (PMF); hydrogen bond (HB); solvent accessible surface area (SASA)

Introduction

Experimental studies performed within the last decades remarkably updated our understanding for biological importance of aggregation formation of biological molecules. Critical biological events (*e.g.*, the gene transcription, protein synthesis, and signal transduction) progress through the aggregate formation and dissolution[1-5], thus denoting that disorder of the functional protein aggregates can directly lead to serious diseases. Nonetheless, we have not sufficiently understood how such aggregates form and function in the cell, even for the paradigmatic molecular species such as amyloid β protein.

Over the past 40 years, formation mechanisms of protein aggregates and the biological roles have been widely examined with regard to serious neurodegenerative diseases such as Alzheimer and Parkinson diseases[6]. Since anomalous protein aggregates are supposed to be pathogenic causes of these diseases, one representative subject is the understanding of pathogenic amyloid fibril formation[7]. Then, it has been one of the central problems how we can suppress formation of pathogenic amyloid fibrils, with the aim of developing therapeutic strategy for these serious diseases[8,9].

To understand the aggregate formation process at molecular level, the kinetic models of aggregate formation have been extensively studied and established[10-12]. Amyloid fibril growth starts from accumulation of sufficient amounts of growth nuclei species, which

are found among the repertoire of oligomeric assembly of proteins and are classified into fibril-like, growth-competent aggregates[11]. This molecule-level mechanism of amyloid fibril formation indicates that clarifying the minimum size of growth nuclei species is a landmark knowledge to understand physicochemical mechanisms of dramatic progress of pathogenic amyloid formation.

To solve the problem, nano-scale observation techniques have been widely employed to observe oligomerization processes in single molecule-level resolution[13-15]. As a technical counterpart to give microscopic insights, theoretical simulations have been extensively employed and have revealed key atomistic interactions acting on aggregate-prone proteins through their aggregation process.[16] These studies have mainly focused on amyloid proteins themselves, which work as building blocks of aggregates and form specific interaction acting among fibril-growth competent monomers.

Besides such specific interactions acting among amyloid proteins in fibril-like shapes, it has been suggested that protein crowding milieus, which consist of the same amyloid protein and form non-fibril, micelle-like shape, also contribute to stable formation of growth nuclei, which has been discussed by several experimental studies for the paradigmatic amyloid peptide, amyloid β (1-42) ($A\beta_{42}$) within the past two decades[17-21].

However, the mechanisms of aggregate crowding milieu for stable formation of growth

nuclei have not been sufficiently elucidated, due to technical difficulty to experimentally capture the molecular structure and dynamics. The emergence of such $A\beta_{42}$ aggregate crowding milieu is transient during amyloid aggregates formation process, then often being out of time resolution of experimental observations. Besides, the crowding milieus are essentially heterogeneous ensemble of conformationally disordered $A\beta_{42}$ monomers, thus being challenging to determine the atomic structures of aggregate crowding milieus so far. Recalling these molecular natures of aggregate crowding milieus, we could suppose atomistic simulations as a feasible, computational counterpart to consider the problem.

In the present study, we examine the effects of $A\beta_{42}$ aggregate crowding milieu on $A\beta_{42}$ stable formation of $A\beta_{42}$ growth nuclei and the microscopic origin. We start from testing the speculation, which we made in the previous study[21]: an $A\beta_{42}$ aggregate crowding milieu suppresses $A\beta_{42}$ monomer dissociations from a growth edge of $A\beta_{42}$ growth nuclei and prevents disassembly of the growth nuclei. To overcome the above experimental difficulty, we theoretically modeled the atomic configuration of $A\beta_{42}$ aggregate milieu by employing the hybrid Monte Carlo/Molecular Dynamics (MC/MD) approach, which we had developed to examine dynamic processes of multimeric proteins[22,23]. By using the simulation-derived $A\beta_{42}$ aggregate milieu systems for the free energy calculation of $A\beta_{42}$

monomer dissociation from the protomer dimer, we confirmed the stabilization effect of $A\beta_{42}$ aggregate milieus on $A\beta_{42}$ growth nuclei formation via $A\beta_{42}$ suppressing monomer dissociation from the growth edge.

Methods

Setup of amyloid-β (1-42) protomer dimer systems

We used the cryogenic electron microscopy (cryo-EM) structure (PDB entry: 5OQV) [24] to construct amyloid-β (1-42), $A\beta_{42}$, 25-mer protomer dimer systems (**Figure 1A**); a protomer denotes an $A\beta_{42}$ oligomer composed of $A\beta_{42}$ monomers in fibril growth-competent conformation. We considered the 50 $A\beta_{42}$ monomers by recalling the earlier studies which reports the number range of $A\beta_{42}$ monomer in the non-fibril aggregates milieu[18-20]. This model is annotated by $A\beta_{42}$(25:25) or simply 25:25, hereafter. We designed $A\beta_{42}$(25:25) in this study, by recalling the earlier experimental studies which reported that a micelle-like $A\beta_{42}$ aggregate consists of 25 to 50 $A\beta_{42}$ monomers[18,19]. Although there is another full-length $A\beta_{42}$ fibril structure (PDB entry: 2NAO[25]), we selected this 5OQV structure by considering the relationship with our earlier studies[21,26].

Nε protonation state was employed for each of histidine residues, and all carboxyl groups in aspartate and glutamate residues were set to the deprotonated state. $A\beta_{42}$(25:25)

was solvated in the 138 Å × 138 Å × 180 Å rectangular box, and 97330 water molecules were finally included in the box. Furthermore, 150 K^+ molecules were added to the solvated system to electrically neutralize the system. Since we are interested in suppression effect of $A\beta_{42}$-crowding milieu on monomer dissociation from $A\beta_{42}$ oligomer (**Figure 1B**), no biological co-solutes were added into aqueous solution except for the counter ions to electronically neutralize these molecular systems. The additional detail for system construction is described in Supporting Information (see **SI-1**).

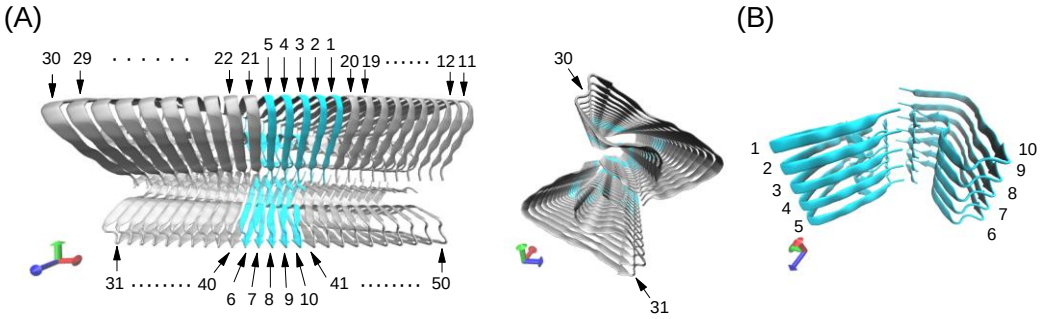

Figure 1. Amyloid β (1-42) 25-mer protomer dimer. (A) the 40 subunits to construct aggregate milieu, and the 5-mer dimers for model of amyloid fibril growth nuclei (referred to as $A\beta_{42}$(5:5)), which are colored with gray and cyan, respectively. Each of the 50 monomers is numbered for the following discussion. (B) $A\beta_{42}$(5:5) whose fibril growth edges are annotated by 1, 5, 6 and 10.

Simulation setup

Molecular mechanics (MM) and molecular dynamics (MD) simulations were performed under the periodic boundary condition with GPU-version PMEMD module in AMBER 17 package[27] based on SPFP algorism[28] with NVIDIA GeForce GTX1080 Ti. Electrostatic interaction was treated by the Particle Mesh Ewald method, where the real space cutoff was set to 0.9 nm. The vibrational motions associated with hydrogen atoms were frozen by SHAKE algorithm through MD simulations. The translational center-of-mass motion of the whole system was removed by every 500 steps to keep the whole system around the origin, avoiding an overflow of coordinate information from the MD trajectory format. To calculate the forces acting among atoms, AMBER force field 14SB[29], TIP3P water model[30,31], and JC ion parameters adjusted for the TIP3P water model[32,33] were used for amino acid residues, water molecules, and ions, respectively. Molecular modeling of each $A\beta_{42}$(N:N) system was performed using the LEaP modules in AmberTools 17 package[27]. These simulation conditions mentioned above were common in all of the simulations discussed in this manuscript.

Unbiased MD simulations

Following temperature and density relaxation simulations, 10-ns NPT MD simulations

(300 K, 1 bar) were performed and used for following analyses. In the present study, we employed this simulation time length for conformation relaxation of $A\beta_{42}$ protomer dimers via transfer from solid phase to liquid phase.

The system temperature and pressure were regulated with Berendsen thermostat[26] with a 5-ps of coupling constant and Monte Carlo barostat with attempt of system volume change by every 100 steps, respectively. A set of initial atomic velocities was randomly assigned from the Maxwellian distribution at 0.001 K at the beginning of the NVT simulations. The time step of integration was set to 2 fs. The further details are shown in Supporting Information (see **SI-2**).

Modeling amyloid aggregate milieu with hybrid MC/MD simulation

The 40 monomers, which are the part of $A\beta_{42}$(25:25), are dissociated to prepare amyloid aggregate milieu by repetitive steered MD simulations. The sequential dissociations of monomers were carried out in the framework of hybrid MC/MD method, which we employed to study disassembly processes of the homomeric protein multimer[22].

In the first 100 hybrid MC/MD cycles, a set of the four monomers at the fibril growth edges (numbered by 11, 30, 31 and 50 in **Figure 1A**) are considered for dissociation. In the next 100 hybrid MC/MD cycles, another set of four monomers (numbered by 12, 29,

32 and 49), which make contacts with the 11, 30, 31 and 50 monomers, are dissociated. Such a simulation procedure was repeated by changing a set of four monomer (see **Table 1** for simulation setup for each of the hybrid MC/MD simulations) until $A\beta_{42}$(5:5) is left in the aqueous solution. As for the monomers making contacts with $A\beta_{42}$(5:5) (numbered by 20, 21, 40 and 41), we employed 400 hybrid MC/MD cycles. This sequential dissociation procedure is designed due to such a physicochemical intuition that an $A\beta_{42}$ monomer at the growth edge is dissociated from $A\beta_{42}$ growth nuclei more frequently than that in the growth nuclei, which is stacked by two neighboring $A\beta_{42}$ monomer.

Inter-$A\beta_{42}$ monomer dissociation was simulated by using steered MD method with force constant of 4.184 kJ/mol/nm^2. A steered force was set along the distance between the centers of mass of given $A\beta_{42}$ monomer pair. At each hybrid MC/MD cycle, a pair of $A\beta_{42}$ monomers is randomly selected among the candidates shown in **Table 1**. The center of mass (COMs) of $A\beta_{42}$ monomer is defined by using 42 $C\alpha$ atoms of the $A\beta_{42}$ monomer.

Table 1. hybrid MC/MD simulation setup for modeling $A\beta_{42}$ aggregate milieu system.

hcbMC/MD simulation order	number of cycle	†monomer pairs undergoing dissociation
1	100	11-12; 30-29; 31-32; 50-49
2	100	12-13; 29-28; 32-33; 49-48
3	100	13-14; 28-27; 33-34; 48-47
4	100	14-15; 27-26; 34-35; 47-46
5	100	15-16; 26-25; 35-36; 46-45
6	100	16-17; 25-24; 36-37; 45-44
7	100	17-18; 24-23; 37-38; 44-43
8	100	18-19; 23-22; 38-39; 43-42
9	100	19-20; 22-21; 39-40; 42-41
10	400	20-1; 21-5; 40-6; 41-10

† For each monomer pair connected by hyphen, a digit at the left side is assigned to $A\beta_{42}$ monomer at the edge of growth axis. A digit is assigned to $A\beta_{42}$ monomer as defined in Figure 1.

Finally, we obtained the snapshot structure of $A\beta_{42}$(5:5) surrounded by an $A\beta_{42}$ aggregate milieu. This snapshot structure is annotated by $A\beta_{42}$(M), where M denotes a milieu. Using $A\beta_{42}$(M), we performed the 100-ns NPT simulation to relax atomistic interaction between $A\beta_{42}$(5:5) and $A\beta_{42}$ aggregate milieu. The simulation result is annotated by $A\beta_{42}$(R|M), where R denotes the relaxation of the $A\beta_{42}$ with aggregate milieu system.

We also construct $A\beta_{42}$(5:5) isolated in aqueous solution by removing the 40 dissociated $A\beta_{42}$ monomers and 120 K^+ ions; this snapshot structure is annotated by $A\beta_{42}$(P), where P denotes pure water. The system density was equilibrated by 10 ns-NPT MD simulation. During the above simulation, we fix $A\beta_{42}$(5:5) conformation around that in $A\beta_{42}$(M) with the aim of fairly evaluating the effect of presence of $A\beta_{42}$ aggregate milieus, where harmonic positional restraints with force constant of 20.92 kJ/mol/nm^2 are imposed on the main chain atoms of $A\beta_{42}$ monomers. Since the simulation setup to obtain $A\beta_{42}$(R|M) and $A\beta_{42}$(P) is similar to that for the above 10-ns NPT MD simulation, we do not repeat the explanation here. Further technical details of the hybrid MC/MD simulations and the procedure to prepare $A\beta_{42}$(P) are given in Supporting Information (see **SI-3** and **SI-4**).

Umbrella sampling MD simulation combined with steered MD simulation

The dissociation processes of $A\beta_{42}$ monomer from the fibril growth edge were described by combining a steered molecular dynamics (SMD) simulation with umbrella sampling molecular dynamics (USMD) simulations. We defined the reaction coordinate as inter-COM distance between the dissociation monomer (S10) and the remaining of the $A\beta_{42}$ pentamer (S6, S7, S8 and S9).

An SMD simulation was employed to obtain an atomic trajectory of $A\beta_{42}$ monomer dissociation from the remaining part of the $A\beta_{42}$ pentamer. 1-ns SMD simulation was carried out under constant NPT condition (300 K, 1 bar), where the system temperature and pressure were regulated by Langevin thermostat with 1-ps^{-1} collision coefficient, and Berendsen barostat[34] with a 5-ps coupling constant, respectively. The value of reaction coordinate was gradually changed through the SMD simulations by imposing the harmonic potential with the force constant of 4.184 kJ/mol/nm^2. The remaining part of $A\beta_{42}$(5:5) was restrained around the initial atomic coordinates by imposing harmonic potential with force constant of 4.184 kJ/mol/nm^2 on the heavy atoms in the main chains.

Then, certain numbers of snapshot structures were extracted from the SMD trajectory with 0.1 nm interval along the reaction coordinate and employed for USMD windows (shown in **Tables S1**, **S2** and **S3**). Following temperature relaxation simulations, several nanoseconds-length NVT USMD simulations (300 K) were performed for each of the USMD windows. The system temperature was regulated using Langevin thermostat with 1-ps^{-1} collision coefficient. Each of the last 3-ns USMD trajectories was used to construct a potential of mean force (Convergence of each PMF profile is discussed in **Fig. S1**).

We also performed SMD-combined USMD simulations for an $A\beta_{42}$ monomer, which is a part of amyloid aggregate milieu, S19. The reaction coordinate is the distance between

COMs of the monomer and the $A\beta_{42}$ pentamer containing S10. The setup of USMD windows is discussed in **Tables S4** and **S5**. The other simulation conditions are similar to those for the dissociating simulations of S10.

The further details, such as setup of harmonic potentials for each of USMD simulations, are described in Supporting Information (see **SI-5**). The reasons for selecting S10 and S19 will be explained in Results and Discussion section.

Trajectory analyses

Root mean square deviation (RMSd), hydrogen bond (HB), solvent accessible surface area (SASA) and secondary structure annotation based on DSSP[28] were calculated with the cpptraj module in AmberTools 17 package[27]. We calculated RMSd to the $A\beta_{42}$ protomer dimer structure derived from the cryo-EM model[21,24] using the backbone heavy atoms (i.e., C_α, N, C and O). The geometrical criterion of HB formation is as follows: H-X distance was < 0.35 nm and X-H-Y angle was > 120˚, where X, Y and H denote acceptor, donor and hydrogen atoms, respectively.

Buried SASA is defined by the following formula, SASA(A:B) − SASA(A) − SASA(B), where A and B are a molecule or molecular assembly, and A:B denotes the complex of A and B. Besides, the hydrodynamic radius (R_{hyd}), which is defined as **Eq. 1**

was used to structurally characterize the hMC/MD simulation-derived aggregates.

$$\frac{1}{R_{hyd}} = \frac{1}{N^2}\langle\sum_{i\neq j}\frac{1}{r_{ij}}\rangle \qquad (1)$$

r_{ij} and N denote the distance between the centers of mass of Aβ42 monomers composing an Aβ42 aggregate (indexed by i and j) and the total number of such Aβ42 monomers, respectively.

Each set of USMD trajectories was used to calculate potential of mean force (PMF) with Weighed Histogram Analysis Method (WHAM)[35]. Statistical errors of PMF values, $\sigma_{PMF}(\xi)$, were estimated by employing bootstrapped sampling[36]:

$$\sigma_{PMF}(\xi) = \left[(N_b - 1)^{-1}\sum_{k=1}^{N_b}\left(W_{b,k}(\xi) - \langle W_b(\xi)\rangle\right)^2\right]^{\frac{1}{2}} \qquad (2)$$

Here, N_b, ξ, and $W_{b,k}(\xi)$ denote the number of bootstrap sampling, the reaction coordinate and the value of kth bootstrapped potential of mean force at each point of ξ, respectively. $\langle W_b(\xi)\rangle$ is average over all $W_{b,k}(\xi)$, where the value of N_b is set to 200 according to the previous study[36].

We evaluated spatial extension of Aβ42 monomer dissociating trajectories by using the bundle radius, R_t.

$$R_t = \frac{1}{N}\sum_{i=1}^{N}\left\{\left(\vec{X}_t^i - \langle\vec{X}_t\rangle\right)\cdot\left(\vec{X}_t^i - \langle\vec{X}_t\rangle\right)\right\}^{\frac{1}{2}} \qquad \mathbf{(3)}$$

$\vec{X}_t^i$ is the center of mass coordinate of dissociating monomer, which is calculated from a set of C_α atoms. The superscript, i and subscript, t, denote a simulation index, which

ranges from 1 to N, and the time point in the SMD simulation, respectively. The number of SMD simulation, N, is set to 50 here. The angle parentheses denote average-calculating operation at the time point, *t*, over the *N* independent SMD simulations.

Molecular structures were illustrated using Visual Molecular Dynamics (VMD)[37]. Error bars are calculated from standard error and indicate 95% confidence interval if there is no annotation.

Results and Discussion

Simulation-derived $A\beta_{42}$ aggregate milieu consists of fibril-growth incompetent monomers and makes contacts with amyloid pentamer dimer on the fibril growth edge

We generated $A\beta_{42}$ aggregate milieu around $A\beta_{42}$(5:5) by dissociating 40 monomers from $A\beta_{42}$(25:25) with the hybrid MC/MD method as follows. First, we performed 10-ns NPT MD simulation to relax the $A\beta_{42}$(25:25) structure upon transfer from solid phase to aqueous phase. Within the 10-ns NPT MD simulation, both the $A\beta_{42}$(25:25) appear to be relaxed in terms of RMSd convergence (**Figure 2**). Similarly, we found RMSd convergence for the $A\beta_{42}$(5:5), which is positioned in the middle of the $A\beta_{42}$(25:25) (colored by blue in **Figure 1**) and is employed as a model of the growth nuclei in this study.

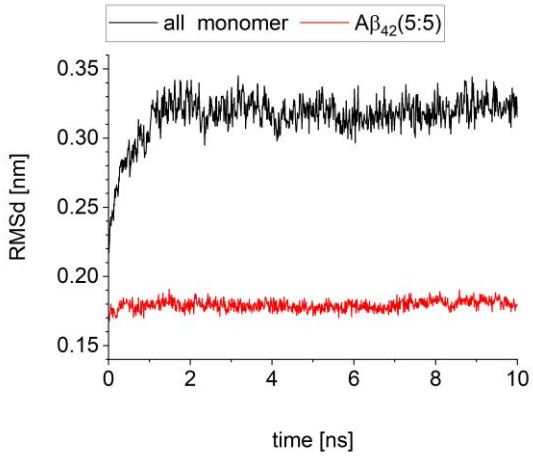

Figure 2. Time course change of root mean square deviation to the experimentally resolved structure. (A) whole of the protofibril, $A\beta_{42}$(25:25) (black line). (B) Pentamer dimer, $A\beta_{42}$(5:5) which is located at the center of the protofibril and colored by blue in **Figure 1** (red line).

Then, we performed the hybrid MC/MD simulations for the10-ns NPT MD snapshot structure and obtained a set of atomic coordinates of $A\beta_{42}$ growth nuclei surrounded by $A\beta_{42}$ aggregate milieu (**Figure 3A**). We annotate the hybrid MC/MD simulation-derived snapshot structure as $A\beta_{42}$(M) hereafter (**Figure 3A**), where the M in the parentheses denotes a 'milieu'.

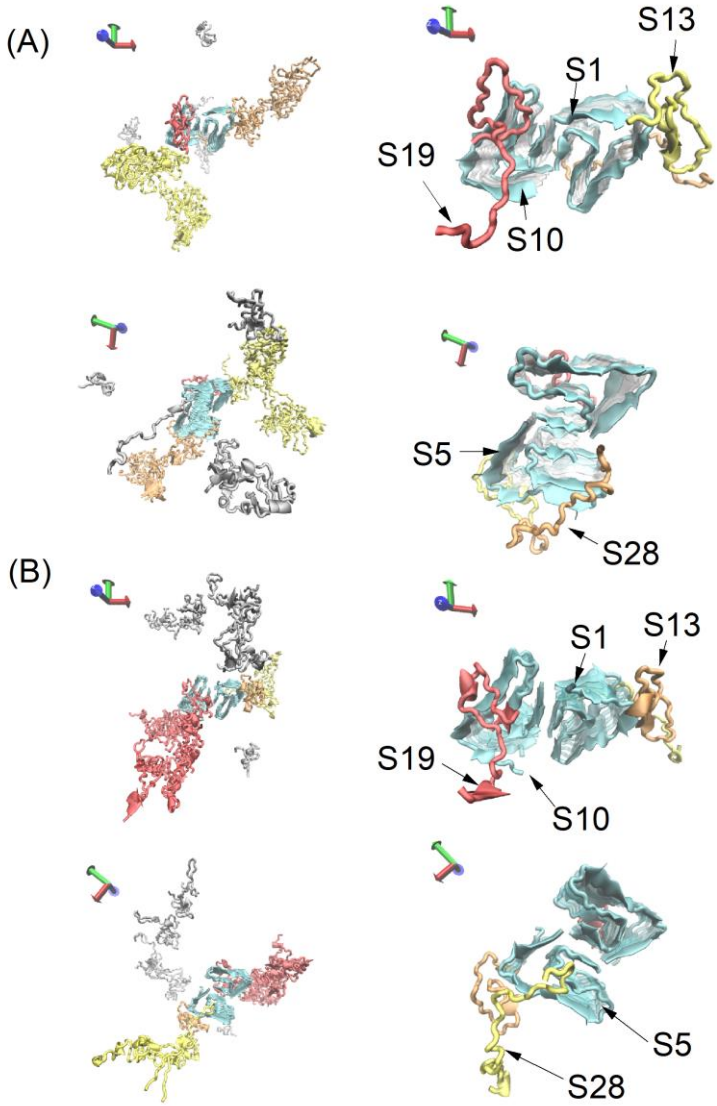

Figure 3. The amyloid β (1-42) (Aβ $_{42}$) pentamer dimer (a model of fibril growth nuclei, Aβ$_{42}$(5:5)) surrounded by the unstructured Aβ$_{42}$ aggregates consisting of 40 monomers. (A) Aβ$_{42}$(M). (B) Aβ $_{42}$(R|M). Aβ$_{42}$(5:5) is colored by cyan. The Aβ$_{42}$ aggregates interacting with Aβ$_{42}$(5:5) are colored by red, yellow and orange. In each of the panels, the whole picture is given in the left, while the monomers which makes contacts with the growth edge of Aβ$_{42}$(5:5) are highlighted in the right.

As remarked in Materials and Methods section, we used $A\beta_{42}$(M) to generate a snapshot structure of $A\beta_{42}$(5:5) in a pure water. We removed a set of atomic coordinates for the 40 $A\beta_{42}$ monomers (indexed from 11 to 50 in **Figure 1A**), which forms aggregate milieu in $A\beta_{42}$(M). This snapshot structure is referred to as $A\beta_{42}$(P), where it is noted that the letter 'P' in the parentheses comes from *pure* water. We can consider this system as a reference to discuss the effect of $A\beta_{42}$ aggregate milieu on suppressing $A\beta_{42}$ monomer dissociation from the fibril growth edge.

We also performed a 100-ns NPT MD simulation for $A\beta_{42}$(M) to relax the interaction between the $A\beta_{42}$ growth nuclei and the $A\beta_{42}$ aggregate milieu. The snapshot structure resulted from the simulation is referred to as $A\beta_{42}$(R|M) (**Figure 3B**), where the letter 'R|M' in the parentheses denotes the relaxation of $A\beta_{42}$(M). Since the number of hydrogen bond (H-bond) formation between $A\beta_{42}$ growth nuclei and $A\beta_{42}$ aggregate milieu is assumed to reach convergence by 20 ns (see **Figure 4**), we use the 100-ns NPT MD snapshot structure to examine the effect of atomistic interaction between $A\beta_{42}$ growth nuclei and $A\beta_{42}$ aggregate milieu on suppressing $A\beta_{42}$ monomer dissociation from the fibril growth edge.

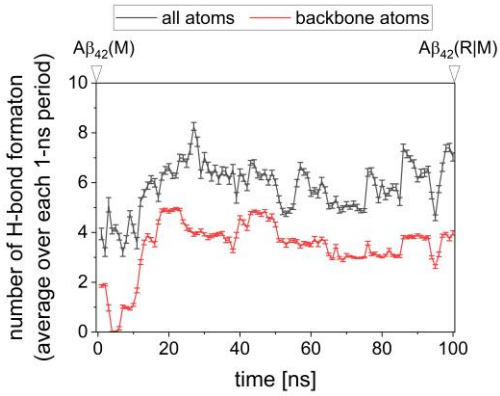

Figure 4. Hydrogen bond (H-bond) formation between Aβ42 growth nuclei (the pentamer dimer) and Aβ42 aggregate milieu (the remaining Aβ42 40 monomers). The black line denotes H-bond calculated for all atoms, while the red line denotes that for backbone atoms. The H-bond number is averaged over each 1-ns period and the error bars indicate 95% confidence interval.

For both of the Aβ42(M) and Aβ42(R|M), the components of the Aβ42 aggregate milieu appear to be off-pathway, fibril-growth incompetent oligomers (**Figure 3A** and **Figure 3B**): they are probably deviated from the amyloid fibril-growth competent form, that is, a LS shape conformation, which is the building block of the Aβ42 fibril structure registered with PDB entry: 5OQV[24]. To confirm this observation, we analyzed the structural properties of Aβ42(5:5) and Aβ42 aggregate milieu consisting of 40 Aβ42 monomers by using the two snapshot structures of Aβ42(M) and Aβ42(R|M). It is noted that Aβ42(P) is

obtained from $A\beta_{42}$(M), thus denoting that the two snapshot structures are enough to discuss structural properties of $A\beta_{42}$ monomer.

We examined secondary structure (SS) annotation for each of 50 $A\beta_{42}$ monomers. The monomers in the $A\beta_{42}$(5:5), indexed from 1 to 10 (*discussed in* **Figure 1**), basically take turn or bent structure around 10th, 25th and 37th residues (see **Figure 5A** and **5B**), indicating that each of these 10 monomers takes the LS shape. The remaining part of the $A\beta_{42}$(5:5) does not show any characteristic SS motifs.

Meanwhile, such SS formation features are not found in some of $A\beta_{42}$ monomers forming the aggregate milieu. The turn and bent structures around 10th, 25th and 37th residues are not necessarily retained for each of the 40 $A\beta_{42}$ monomers, indexed from 11 to 50. Instead, the remaining amino acid residues in each monomer shows additional turn and bent at the other regions, and also helix and strand formations in some cases.

The above analyses support the observation that these 40 $A\beta_{42}$ monomers take forms deviated from the LS shape conformation[24]. We further confirmed this observation by examining the RMSd values to the reference structure, the $A\beta_{42}$ monomer in LS shape conformation shown in **Figure 5C**. The $A\beta_{42}$ monomers in $A\beta_{42}$(5:5) have RMSd value of about 0.2 nm, while each of $A\beta_{42}$ monomers forming $A\beta_{42}$ aggregate milieus shows RMSd value greater than 1 nm (**Figure 6**). According to the above SS and RMSd analyses,

we can say that the components of $A\beta_{42}$ aggregate milieus, which are prepared by using the hybrid MC/MD simulations, are apparently structurally different from each of $A\beta_{42}$ monomers in $A\beta_{42}$(5:5). Thus, we can suppose that these $A\beta_{42}$ monomers form off-pathway, fibril-growth incompetent $A\beta_{42}$ aggregates rather than fibril-growth competent $A\beta_{42}$ oligomer such as $A\beta_{42}$(5:5).

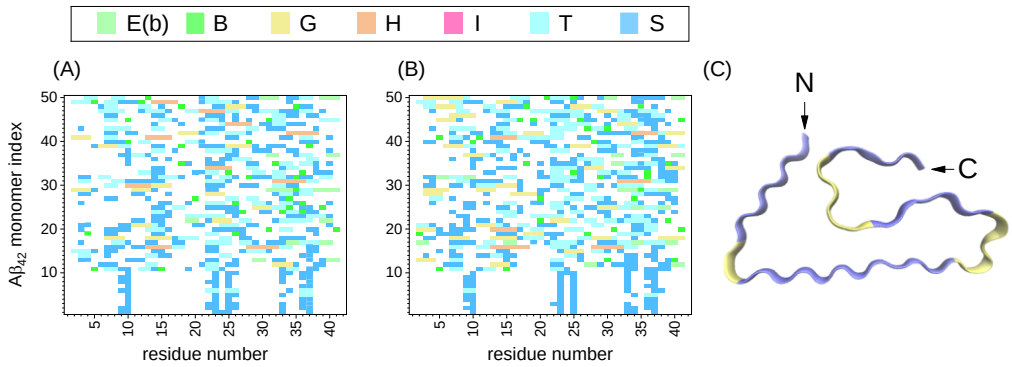

Figure 5. Secondary structure (SS) annotations for Aβ42 monomers. (A) Aβ42(M). (B) Aβ42(R|M). (C) Aβ42 monomer structure in fibril-growth competent form, the LS shape, which is found in the Aβ42 fibril structure registered with PDB entry: 5OQV. With regard to panels A and B, SS annotations are given as single letter format: E(b): extended β; B: isolated β; G: 3-10 helix; H: α helix; I: π(3-14) helix; T: turn; S: bend. In panel C, the letters 'N' and 'C' indicate N- and C-terminals of Aβ42 monomer, respectively. The following residues are involved in turn and bend formation and colored by yellow: Gly9, Thr10, Glu22, Asp23, Val24, Gly25, Ser26, Gly33, Leu34, Met35, Val36, Gly37.

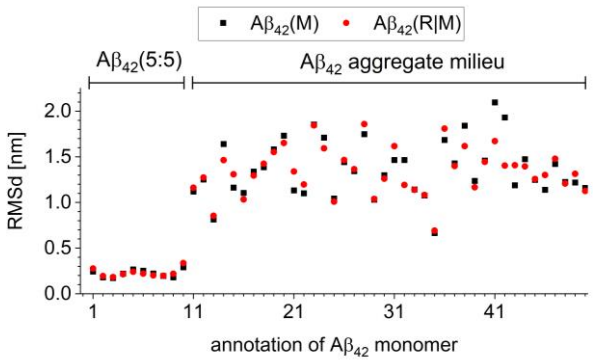

Figure 6. Root mean square deviation (RMSd) from the fibril-growth competent LS shape conformation (a monomer derived from the amyloid fibril deposited as PDB entry: 5OQV). $A\beta_{42}$(M) and $A\beta_{42}$(R|M) are shown by black and red symbols, respectively.

We investigated the number of $A\beta_{42}$ monomer forming each $A\beta_{42}$ aggregate milieu and classified them into two groups with regard to the presence and absence of atomic contacts with $A\beta_{42}$(5:5). The results are summarized in **Table 3** and **Table 4** for $A\beta_{42}$(M) and $A\beta_{42}$(R|M), respectively. It is noted that an annotation with capital letter (*e.g.*, A_1) denotes an aggregate milieu which makes atomic contacts with any of monomers in $A\beta_{42}$(5:5) and that with minuscule letter (*e.g.*, a_1) denotes the aggregate milieu without making atomic contacts with $A\beta_{42}$(5:5).

Table 3. Classification of $A\beta_{42}$ monomers (components 11-50) forming $A\beta_{42}$ aggregate milieu in $A\beta_{42}$(M) system. $A\beta_{42}$ monomers in aggregate milieu, which make atomic contacts with any of monomers in $A\beta_{42}$(5:5) (component 1-10), are highlighted by bold character.

Aggregate	Component
A_1	14,15,16,17,21,22,23,24,25,26,27,40,**42**,43,**44**,45,46,47
A_2	**13**,20,**28**,**29**,32,33,34,35,36,37,38,**48**
a_1	12,30,31,49
A_3	18,**19**
a_2	11,50
a_3	39
a_4	41

Table 4. Classification of $A\beta_{42}$ monomers (components 11-50) forming $A\beta_{42}$ aggregate milieu in $A\beta_{42}$(R|M) system. $A\beta_{42}$ monomers in aggregate milieu, which make atomic contacts with any of monomers in $A\beta_{42}$(5:5) (component 1-10), are highlighted by bold character. The subscript 'r' denotes relaxation by the 100-ns NPT MD simulation.

Aggregate	Component
A_{1r}	14,15,16,17,18,**19**,24,25,26,27,30,31,40,**41**,**42**,43,**44**,45,46,49
a_{1r}	12,35,36,37,38,39
A_{2r}	20,**28**,29,32,33,34
a_{2r}	11,21,22,23,50
A_{3r}	**13**,48

For both of $A\beta_{42}$(M) and $A\beta_{42}$(R|M), $A\beta_{42}$(5:5) makes contacts with seven or six $A\beta_{42}$ monomers in $A\beta_{42}$ aggregate milieu (annotated by bold characters in **Tables 3** and **4**), respectively. This observation indicates that $A\beta_{42}$(5:5) is not encompassed by $A\beta_{42}$ aggregate milieu, but makes local contacts with $A\beta_{42}$ aggregates. In other words, $A\beta_{42}$(5:5) forms a pairwise complex with an $A\beta_{42}$ aggregate.

We also evaluated the global shape of a component of $A\beta_{42}$ aggregate milieu, which has the largest number of $A\beta_{42}$ monomer, A_1 and A_{1r} for $A\beta_{42}$(M) and $A\beta_{42}$(R|M), respectively. The values of hydrodynamic radius (R_{hyd}, which is defined in **eqn. 1**) are 12 and 25 nm for $A\beta_{42}$(M) and $A\beta_{42}$(R|M), respectively. According to the earlier experimental studies, a micelle-like $A\beta_{42}$ aggregate consists of 25 to 50 $A\beta_{42}$ monomers[18,19] and shows value of R_{hyd} in range from 2.4 to 11.4 nm[18]. Thus, we could suppose our simulation-derived aggregate species are not such micelle-like aggregates. These aggregates are less condensed spatially than a micelle-like $A\beta_{42}$ aggregate but are rather extended in the space, as indicated by analyses of R_{hyd}. It is thus noted that we here discuss new facet of $A\beta_{42}$ aggregate milieu effect on stable formation of $A\beta_{42}$ growth nuclei below.

Among the four $A\beta_{42}$ monomers at the fibril growth edge (S1, S5, S6 and S10) of $A\beta_{42}$(5:5), the monomers except for S6 make contacts with any of the $A\beta_{42}$ aggregates

(see **Figure 3**). For the three monomers, we analyzed solvent accessible surface area (SASA) covered by an amyloid aggregate and found that S10 has the greatest buried SASA value of the three $A\beta_{42}$ monomers for both $A\beta_{42}$(M) and $A\beta_{42}$(R|M). Magnitude of the buried SASA possibly correlates with energetic stability of intermolecular interaction. We then supposed that S10 relatively strongly interacts with $A\beta_{42}$ aggregates compared with S1 and S5 and considered the S10 for the free energy calculations of monomer dissociation from the fibril growth edge.

Table 5. Buried solvent accessible surface area for $A\beta_{42}$ monomers in the fibril growth edge of $A\beta_{42}$(5:5) [unit: nm^2]. Monomers in $A\beta_{42}$(5:5) are annotated as in the case of **Figure 1**.

monomer in $A\beta_{42}$(5:5)	$A\beta_{42}$(M)	$A\beta_{42}$(R|M)
S1	7.22	6.88
S5	7.73	6.56
S6	0	0
S10	9.01	17.07

$A\beta_{42}$ aggregate milieu suppresses $A\beta_{42}$ monomer dissociation from the fibril growth edge by anchoring the monomer to $A\beta_{42}$ growth nuclei

We will examine the effects of $A\beta_{42}$ aggregate milieu on $A\beta_{42}$ monomer dissociation processes as follows. First, we performed independent 50 SMD simulations for the $A\beta_{42}$ monomer (S10) dissociation from the fibril growth edge of the $A\beta_{42}$(5:5). Each of the three snapshot structures, $A\beta_{42}$(M), $A\beta_{42}$(P) and $A\beta_{42}$(R|M), was employed as the set of the initial atomic coordinates. It is noted that the simulated results are annotated by the corresponding $A\beta_{42}$ snapshot structure, namely, $A\beta_{42}$(M), $A\beta_{42}$(P) or $A\beta_{42}$(R|M), hereafter.

Figure 7 shows the trajectory of center of mass of the dissociating $A\beta_{42}$ monomer, S10. A set of SMD simulations starting from $A\beta_{42}$(P) shows a broader distribution of the center of mass (COM) of the dissociating $A\beta_{42}$ monomer than those from $A\beta_{42}$(M) and $A\beta_{42}$(R|M). We can obtain this observation by comparing **Fig. 7A-C** with **Fig. 7D-F** and **Fig. 7G-I**.

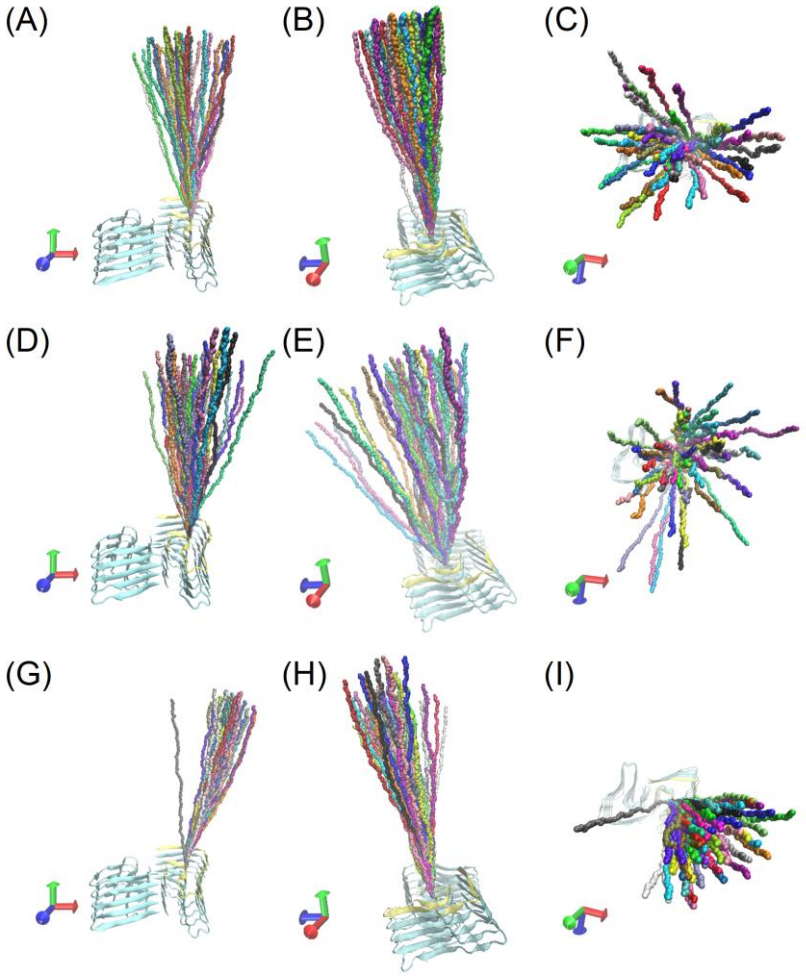

Figure 7. Dissociating pathways of $A\beta_{42}$ monomer from the growth edge. (A)-(C) $A\beta_{42}$(M). (D)-(F) $A\beta_{42}$(P). (G)-(I) $A\beta_{42}$(R|M). Center of mass (COM) of the dissociating $A\beta_{42}$ monomer is represented by colored sphere. Each of the 50 COM trajectories is distinguished by the different color. The dissociation-attempted $A\beta_{42}$ monomer in $A\beta_{42}$(5:5), S10, and the remaining of $A\beta_{42}$(5:5) are represented by yellow and blue ribbon, respectively.

We confirm the above observation by quantitatively characterizing the spatial

expansion of the COM distributions with an effective radius at each time point, which is defined in **eqn. 3**. As shown in **Fig. 8**, along the time course of the SMD simulation, the effective radius for $A\beta_{42}$(M) and $A\beta_{42}$(R|M) is smaller than that for $A\beta_{42}$(P). It can thus be said that the presence of amyloid aggregate milieu spatially restricts dissociation pathways of $A\beta_{42}$ monomer from the edge of growth axis.

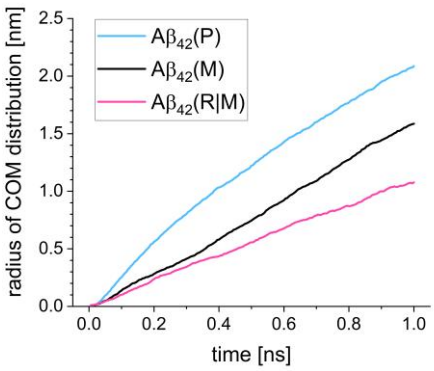

Figure 8. Spatial expansion of $A\beta_{42}$ monomer dissociating trajectory, estimated by the effective radius of dissociating trajectory set (see **eqn. 3** for the definition).

The narrowed distributions of $A\beta_{42}$ monomer dissociation pathways remind us of entropic contribution of $A\beta_{42}$ aggregate milieu to stable formation of $A\beta_{42}$ growth nuclei. The $A\beta_{42}$ aggregate milieu has much larger inertia than water molecules which can move flexibly in the system, so that the milieu could more stably reside at the same place than

water molecules and could reduce the space which the dissociation monomer can access. Therefore, it is straightforward expectation that such a reduction of accessible space prevents $A\beta_{42}$ monomer dissociation with increase of entropic costs.

We tested such entropic effects of $A\beta_{42}$ aggregate milieu on energetic stability of $A\beta_{42}$ monomer binding to the fibril growth axis by calculating free energy profiles of $A\beta_{42}$ monomer dissociation from the fibril growth edge of $A\beta_{42}$(5:5). For each of the three systems, we randomly selected 6 SMD simulations among the 50 ones, and used the six SMD trajectories for individual USMD simulations. As remarked in Materials and Method section, 6 is the minimum to make 200 resampling for bootstrap error estimation; the resampling number of 200 is the commonly used number in this field for bootstrap error estimation[36].

Interestingly, there are no significant difference between $A\beta_{42}$(M) and $A\beta_{42}$(P) in the activation barrier of $A\beta_{42}$ monomer dissociation (see black lines in **Fig. 9A** and **9B**, respectively). The activation barrier of $A\beta_{42}$(P) is 35.2 ± 5.2 kJ/mol, while that of $A\beta_{42}$(M) is 39.6 ± 9.6 kJ/mol. As discussed with regard to **Fig. 8**, the presence of $A\beta_{42}$ aggregate milieu restricted accessible space for the $A\beta_{42}$ monomer, S10, upon the dissociation from the growth edge, then suggesting an entropic cost to increase free energy barrier of the $A\beta_{42}$ monomer dissociation process. However, our free energy calculations result that the

entropic effect discussed in **Fig. 8** does not significantly contributes to Aβ42 monomer binding to the growth edge of Aβ42 oligomer. We could say that an Aβ42 aggregate just surrounding an Aβ42 growth nuclei does not necessarily work for stable formation of Aβ42 growth nuclei.

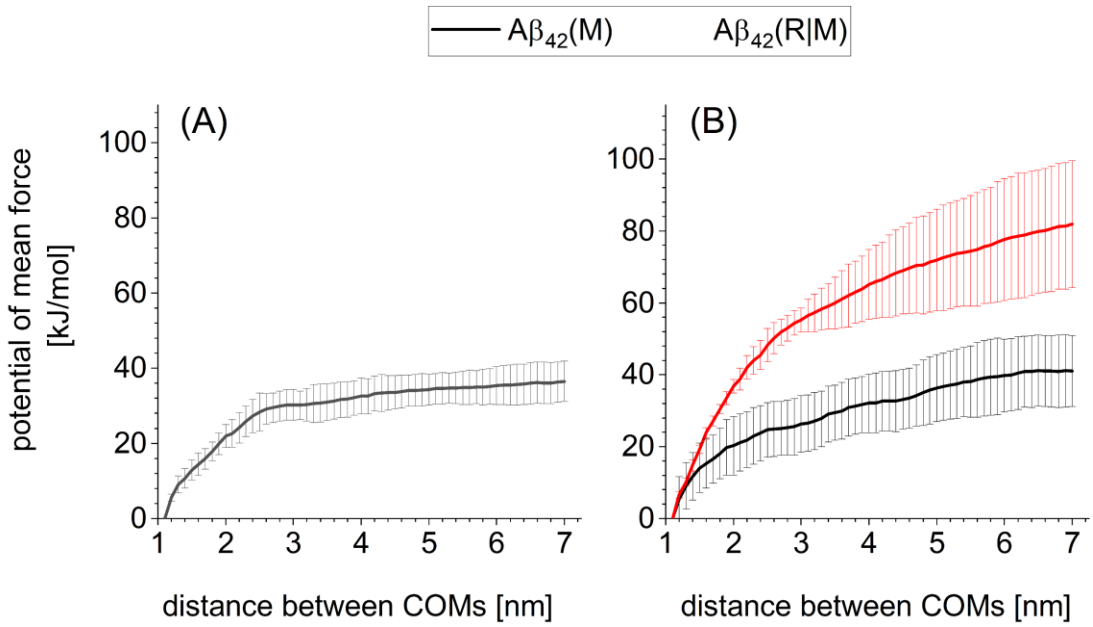

Figure 9. Potential of mean force for Aβ42 monomer dissociation from the fibril growth edge of pentameric oligomer. (A) Aβ42(5:5) in aqueous solution, Aβ42(P). (B) Aβ42(5:5) in Aβ42 crowding milieu. In the panel B, black and red lines are for Aβ42(M) and Aβ42(R|M), respectively.

Meanwhile, there are significant difference between Aβ42(R|M) and the other two Aβ42

systems in $A\beta_{42}$ monomer binding to the growth edge: the activation barrier is 82.4 ± 17.2 kcal/mol (see red line in **Fig. 9B**). The significant difference between $A\beta_{42}$(M) and $A\beta_{42}$(R|M) suggests the microscopic origin of roles of $A\beta_{42}$ amyloid aggregate in thermodynamically stabilizing $A\beta_{42}$ monomer binding, that is, enthalpic stabilization with direct atomistic interaction with an $A\beta_{42}$ amyloid growth nuclei such as $A\beta_{42}$(5:5). It is worthwhile noting that in $A\beta_{42}$(R|M), a monomer in the amyloid aggregate milieu, S19, makes atomic contacts with both the dissociating monomer, S10, and the remaining of $A\beta_{42}$(5:5) (**Fig. 10**). This observation lets us suppose that the S19 anchors S10 on the remaining of $A\beta_{42}$(5:5) and cooperatively suppresses S10 dissociation from the growth edge.

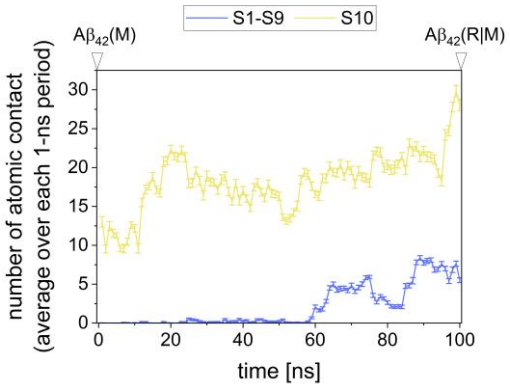

Figure 10. Atomic contacts of S19 with S10 and the remaining of Aβ42(5:5), nine monomers from S1 to S9, shown by yellow and blue lines, respectively. The atomic contact number is averaged over each 1-ns period and the error bars indicate 95% confidence interval.

If such anchoring effect works for suppression of S10 dissociation, S19 in Aβ42(R|M) maybe more strongly interacts with Aβ42(5:5) than in Aβ42(M). To verify this speculation, we examined the dissociation free energy landscape for S19. As the initial structures for free energy landscape calculations, we used the hybrid MC/MD-derived configuration and the subsequent 100-ns NPT MD derived configuration, which are discussed in **Figure 4A** and **4B** as Aβ42(M) and Aβ42(R|M), respectively.

By comparing the free energy landscapes between Aβ42(R|M) and Aβ42(M), we can find that Aβ42(R|M) has a greater PMF value than Aβ42(M) (see **Fig. 11**). As for Aβ42(M),

the height of activation barrier is less than 8 kJ/mol. Meanwhile, Aβ42(R|M) shows an up-hill shape of the free energy landscape and has ca 32 kJ/mol at 8 nm. The S19 more stably interacts with the Aβ42(5:5) in Aβ42(R|M), due to the greater number of atomic contacts (see **Fig. 10**), than in Aβ42(M). S19 of Aβ42(R|M) appears to loosely bind to Aβ42(5:5) with relatively weak interaction in comparison with the S10 interaction with Aβ42(5:5), while such loose interaction with Aβ42(5:5) may be sufficient to cooperatively suppress Aβ42 monomer dissociation from the growth edge (see **Fig. 9B**).

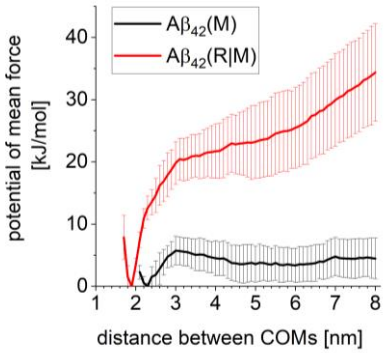

Figure 11. Potential of mean force for aggregate milieu component Aβ42 monomer (S19) dissociation from the Aβ42(5:5). Black and red lines are for Aβ42(M) and Aβ42(R|M), respectively.

Concluding Remarks

In the present study, we discussed roles of the $A\beta_{42}$ aggregate milieu in stable formation of $A\beta_{42}$ growth nuclei by employing atomistic molecular dynamics simulations. We found that off-pathway, fibril-growth incompetent oligomeric $A\beta_{42}$ aggregates directly interact with both dissociating $A\beta_{42}$ monomer and the remaining of the growth nuclei and suppress the monomer dissociation by significant increase of the height of activation barrier in the process. We can suppose that such $A\beta_{42}$ aggregates enthalpically stabilizes and progresses growth nuclei formation by loosely but cooperatively binding to the growth nuclei and dissociation-prone monomer at the edge of the growth nuclei. Although our observation for the effect of $A\beta_{42}$ aggregate crowding milieu is obtained from one hybrid MC/MD simulation-derived $A\beta_{42}$ aggregates structure, the microscopic mechanism proposed on the basis of the observation appears to be independent of specific atomistic details of aggregate crowding milieus. Thus, we may suppose that it is worthwhile to consider the mechanism for other amyloid aggregate milieus.

It is also worthwhile to remark that our simulation-derived $A\beta_{42}$ aggregates do not take a micelle-like form but rather appear to take unstructured and spatially expanded configurations. It has been considered that micelle-like $A\beta_{42}$ aggregates play important roles in $A\beta_{42}$ fibril formation[17-20]. Besides this conventional observation, we newly

propose that off-pathway, fibril-growth incompetent, non-micelle-like $A\beta_{42}$ aggregates can contribute to stable formation of $A\beta_{42}$ growth nuclei by suppressing $A\beta_{42}$ monomer dissociation. It is reported that ATP molecules in physiological concentration nonspecifically dissolve protein aggregates including $A\beta_{42}$ aggregates[26,38]. Recalling the roles of $A\beta_{42}$ aggregate milieu in stable formation of $A\beta_{42}$ aggregate growth nuclei, we speculate that ATP molecules suppress formations of both fibril-like aggregates and aggregate milieus simultaneously to preserve healthy cell conditions. Nonetheless, it is beyond the scope of this study to test the speculation, thus being left for future study.

Supporting Information

The Supporting Information is available. Detailed procedures for unbiased MD, SMD and USMD simulations, Figures and Tables for analyses of these simulations.

Acknowledgements

This work was supported by a Grant-Aid for Scientific Research on Innovative Areas "Chemistry for Multimolecular Crowding Biosystems" (JSPS KAKENHI Grand No. JP17H06353) and by MEXT Quantum Leap Flagship Program (Grant No. JPMXS0120330644).

Author Information

Corresponding Authors

Ikuo Kurisaki - Waseda Research Institute for Science and Engineering, Waseda University, Tokyo 169-8555, Japan; ORCID: 0000-0003-4519-1093; Email: ikuo.kurisaki@aoni.waseda.jp

Shigenori Tanaka - Graduate School of System Informatics, Kobe University, 1-1 Rokkodai, Nada-ku, Kobe 657-8501, Japan; ORCID: 0000-0002-6659-2788; Email: tanaka2@kobe-u.ac.jp

References

1. Shin Y, Brangwynne CP. Liquid phase condensation in cell physiology and disease. *Science.* 2017;357:4382.

2. Wheeler RJ, Hyman AA. Controlling compartmentalization by non-membrane-bound organelles. *Philos T R Soc B.* 2018;373:201170193.

3. Hofmann S, Kedersha N, Anderson P, Ivanov P. Molecular mechanisms of stress granule assembly and disassembly. *Bba-Mol Cell Res.* 2021;1868:118876.

4. Kang JY, Wen Z, Pan D, et al. LLPS of FXR1 drives spermiogenesis by activating

translation of stored mRNAs. *Science.* 2022;377:6477.

5. Yan VT, Narayanan A, Wiegantr T, Julicher F, Grill SW. A condensate dynamic instability orchestrates actomyosin cortex activation. *Nature.* 2022;609:597-604.

6. Chiti F, Dobson CM. Protein misfolding, functional amyloid, and human disease. *Annu Rev Biochem.* 2006;75:333-366.

7. Chiti F, Dobson CM. Protein Misfolding, Amyloid Formation, and Human Disease: A Summary of Progress Over the Last Decade. *Annu Rev Biochem.* 2017;86:27-68.

8. Selkoe DJ, Hardy J. The amyloid hypothesis of Alzheimer's disease at 25years. *Embo Mol Med.* 2016;8:595-608.

9. Tolar M, Abushakra S, Sabbagh M. The path forward in Alzheimer's disease therapeutics: Reevaluating the amyloid cascade hypothesis. *Alzheimers Dement.* 2020;16:1553-1560.

10. Cohen SIA, Linse S, Luheshi LM, et al. Proliferation of amyloid-beta 42 aggregates occurs through a secondary nucleation mechanism. *P Natl Acad Sci USA.* 2013;110:9758-9763.

11. Knowles TPJ, Waudby CA, Devlin GL, et al. An Analytical Solution to the Kinetics of Breakable Filament Assembly. *Science.* 2009;326:1533-1537.

12. Owen MC, Gnutt D, Gao MM, et al. Effects of in vivo conditions on amyloid aggregation. *Chem Soc Rev.* 2019;48:3946-3996.

13. Watanabe-Nakayama T, Ono K, Itami M, Takahashi R, Teplow DB, Yamada M. High-speed atomic force microscopy reveals structural dynamics of amyloid beta(1-42) aggregates. *P Natl Acad Sci USA.* 2016;113:5835-5840.

14. Bode DC, Freeley M, Nield J, Palma M, Viles JH. Amyloid- oligomers have a profound detergent-like effect on lipid membrane bilayers, imaged by atomic force and electron microscopy. *J Biol Chem.* 2019;294:7566-7572.

15. Feng L, Watanabe H, Molino P, et al. Dynamics of Inter-Molecular Interactions Between Single A beta(42) Oligomeric and Aggregate Species by High-Speed Atomic Force Microscopy. *J Mol Biol.* 2019;431:2687-2699.

16. Nguyen PH, Ramamoorthy A, Sahoo BR, et al. Amyloid Oligomers: A Joint Experimental/Computational Perspective on Alzheimer's Disease, Parkinson's Disease, Type II Diabetes, and Amyotrophic Lateral Sclerosis. *Chem Rev.* 2021;121:2545-2647.

17. Lomakin A, Chung DS, Benedek GB, Kirschner DA, Teplow DB. On the nucleation and growth of amyloid beta-protein fibrils: Detection of nuclei and quantitation of rate constants. *P Natl Acad Sci USA.* 1996;93:1125-1129.

18. Yong W, Lomakin A, Kirkitadze MD, Teplow DB, Chen SH, Benedek GB. Structure determination of micelle-like intermediates in amyloid beta-protein fibril assembly by using small angle neutron scattering. *P Natl Acad Sci USA.* 2002;99:150-154.

19. Sabate R, Estelrich J. Evidence of the existence of micelles in the fibrillogenesis of beta-amyloid peptide. *Journal of Physical Chemistry B.* 2005;109:11027-11032.

20. Novo M, Freire S, Al-Soufi W. Critical aggregation concentration for the formation of early Amyloid-beta (1-42) oligomers. *Sci Rep-Uk.* 2018;8:1783.

21. Kurisaki I, Tanaka S. Remarked suppression of $A\beta_{42}$ protomer-protomer dissociation reaction elucidated by molecular dynamics simulation. *Proteins.* 2022;90:1367-1375.

22. Kurisaki I, Tanaka S. Reaction Pathway Sampling and Free-Energy Analyses for Multimeric Protein Complex Disassembly by Employing Hybrid Configuration Bias Monte Carlo/Molecular Dynamics Simulation. *Acs Omega.* 2021;6:4749-4758.

23. Kurisaki I, Tanaka S. Computational prediction of heteromeric protein complex disassembly order using hybrid Monte Carlo/molecular dynamics simulation. *Phys Chem Chem Phys.* 2022;24:10575-10587.

24. Gremer L, Scholzel D, Schenk C, et al. Fibril structure of amyloid-beta(1-42) by cryo-electron microscopy. *Science.* 2017;358:116-119.

25. Wolff M, Zhang-Haagen B, Decker C, et al. $A\beta_{42}$ pentamers/hexamers are the smallest detectable oligomers in solution. *Sci Rep-Uk.* 2017;7:2493.

26. Kurisaki I, Tanaka S. ATP Converts A beta(42) Oligomer into Off-Pathway Species by Making Contact with Its Backbone Atoms Using Hydrophobic Adenosine. *Journal of Physical Chemistry B.* 2019;123:9922-9933.

27. *Case DA, Cerutti DS, Cheatham TE III, et al. Amber 17. University of California; 2017.*

28. Le Grand S, Gotz AW, Walker RC. SPFP: Speed without compromise-A mixed precision model for GPU accelerated molecular dynamics simulations. *Comput Phys Commun.* 2013;184:374-380.

29. Maier JA, Martinez C, Kasavajhala K, Wickstrom L, Hauser KE, Simmerling C. ff14SB: Improving the Accuracy of Protein Side Chain and Backbone Parameters from ff99SB. *J Chem Theory Comput.* 2015;11:3696-3713.

30. Jorgensen WL, Chandrasekhar J, Madura JD, Impey RW, Klein ML. Comparison of simple potential functions for simulating liquid water. *J Chem Phys.* 1983;79:926-935.

31. Kusalik PG, Svishchev IM. The Spatial Structure in Liquid Water. *Science.* 1994;265:1219-1221.

32. Joung IS, Cheatham TE. Determination of alkali and halide monovalent ion parameters for use in explicitly solvated biomolecular simulations. *J Phys Chem B.* 2008;112:9020-9041.

33. Joung IS, Cheatham TE, III. Molecular Dynamics Simulations of the Dynamic and Energetic Properties of Alkali and Halide Ions Using Water-Model-Specific Ion Parameters. *J Phys Chem B.* 2009;113:13279-13290.

34. Berendsen HJC, Postma JPM, Vangunsteren WF, Dinola A, Haak JR. Molecular-dynamics with coupling to an external bath. *J Chem Phys.* 1984;81:3684-3690.

35. Kumar S, Bouzida D, Swendsen RH, Kollman PA, Rosenberg JM. The weighted histogram analysis method for free-energy calculations on biomolecules .1. The method. *J Comput Chem.* 1992;13:1011-1021.

36. Hub JS, de Groot BL, van der Spoel D. g_wham-A free weighted histogram analysis implementation including robust error and autocorrelation estimates. *J Chem Theory Comput.* 2010;6:3713-3720.

37. Humphrey W, Dalke A, Schulten K. VMD: Visual molecular dynamics. *J Mol Graphics Modelling.* 1996;14:33-38.

38. Patel A, Malinovska L, Saha S, et al. ATP as a biological hydrotrope. *Science.* 2017;356:753-756.